

PAPER • OPEN ACCESS

# Characterization of strongly coupled plasmas produced in argon supercritical fluids

To cite this article: Seungtaek Lee *et al* 2022 *Plasma Phys. Control. Fusion* **64** 095010

View the [article online](#) for updates and enhancements.

## You may also like

- [Various shape memory effects of stimuli-responsive shape memory polymers](#)  
Harper Meng, Habib Mohamadian, Michael Stubblefield et al.
- [The brain's resonance with breathing—decelerated breathing synchronizes heart rate and slow cortical potentials](#)  
Thilo Hinterberger, Nike Walter, Christopher Doliwa et al.
- [THE NORTHERN WRAPS OF THE SAGITTARIUS STREAM AS TRACED BY RED CLUMP STARS: DISTANCES, INTRINSIC WIDTHS, AND STELLAR DENSITIES](#)  
M. Correnti, M. Bellazzini, R. A. Ibata et al.

# Characterization of strongly coupled plasmas produced in argon supercritical fluids

Seungtaek Lee<sup>1,2,5</sup> , Juho Lee<sup>1,5</sup> , Young Dae Yoon<sup>3</sup> , Dong Eon Kim<sup>1,4,\*</sup> and Gunsu Yun<sup>1,2,4,\*</sup> 

<sup>1</sup> Department of Physics, POSTECH, Pohang, Republic of Korea

<sup>2</sup> Division of Advanced Nuclear Engineering, POSTECH, Pohang, Republic of Korea

<sup>3</sup> Pohang Accelerator Laboratory, POSTECH, Pohang, Republic of Korea

<sup>4</sup> Max Planck Center for Attosecond Science, Max Planck POSTECH/KOREA Research Initiative, Pohang, Republic of Korea

E-mail: [kimd@postech.ac.kr](mailto:kimd@postech.ac.kr) and [gunsu@postech.ac.kr](mailto:gunsu@postech.ac.kr)

Received 18 March 2022, revised 14 June 2022

Accepted for publication 6 July 2022

Published 25 July 2022



## Abstract

Strongly coupled plasmas (SCPs) exist in various places throughout the Universe, examples of which are inertial confinement fusion experiments, Jovian planets' cores, neutron stars, and white dwarf stars. In recent decades, theoretical and numerical studies have been pursued to characterize the equation of states and thermodynamic properties of SCPs, which are fundamentally different from those of weakly coupled plasmas. One of the essential research topics is energy transport by radiation or opacity. In particular, in a subcritical medium at a low temperature, condensation renders the medium inhomogeneous, which significantly affects the radiation transport or opacity. However, no study has been conducted for opacity in inhomogeneous supercritical fluids (SCFs). A recent study reveals that an inhomogeneous SCF with nanometer-sized clusters and micrometer-sized droplets can be prepared. Here, we experimentally demonstrate that the emission timescale of an SCP in an inhomogeneous SCF is extended by up to 50% compared to that in a homogeneous SCF. This implies that the inhomogeneity of the SCF significantly enhances the photon confinement. This result is expected to draw interest in the investigation of radiation transport or opacity in the inhomogeneous SCF. A better understanding will lead to a method for increasing the brightness and light emission time from a dense plasma.

Supplementary material for this article is available [online](#)

Keywords: laser produced plasma, strongly coupled plasma, inhomogeneous supercritical fluid, equation of state

(Some figures may appear in colour only in the online journal)

<sup>5</sup> These authors contributed equally.

\* Authors to whom any correspondence should be addressed.



Original Content from this work may be used under the terms of the [Creative Commons Attribution 4.0 licence](#). Any further distribution of this work must maintain attribution to the author(s) and the title of the work, journal citation and DOI.

## 1. Introduction

Strongly coupled plasmas (SCPs) are plasmas in which the average Coulomb potential energy of the interacting particles exceeds their average thermal kinetic energy. For electrons, the coupling parameter is defined as  $\Gamma = (e^2/4\pi\epsilon_0 k_B T_e)(4\pi n_e/3)^{1/3}$ , where  $e$ ,  $\epsilon_0$ ,  $k_B$ ,  $T_e$ , and  $n_e$  are the electron charge, vacuum permittivity, Boltzmann constant, the electron temperature, and the electron density, respectively. Standard theories for an ideal plasma fail to describe strongly-correlated systems with  $\Gamma \gtrsim 1$  [1, 2]. Unlike ideal plasmas, the Debye shielding assumption fails in SCPs. Furthermore, as  $\Gamma$  increases, the plasma differs from the gaseous behavior and exhibits liquid or solid characteristics. The short-range order interaction between particles makes the theoretical approach to SCP challenging. The plasma may undergo the Wigner crystallization when the  $\Gamma$  exceeds  $\sim 180$  [1, 3]. Recently, there have been efforts to calculate structural and thermodynamic properties for SCPs with high  $\Gamma$  values [3]. More importantly, SCPs are encountered in many contexts such as galaxies, white dwarf stars, cores of Jovian planets [4], lightning in thick planetary atmospheres [5], and inertial confinement fusion experiments [6].

Owing to their scientific importance and possible practical applications of SCPs, significant efforts have been made for several decades to study thermodynamic properties of SCPs, in particular, the equation of states, which connects the thermodynamic quantities of the plasma such as internal energy density and pressure [7]. However, experimental determination of equation of states is still challenging due to the short time scales of most SCP experiments. The radiation transport in SCPs is also considered important for understanding energy transport during star formation in an accretion disk and nuclear burning in the core of the star. The opacity, which is a convenient measure of the resistance to the transmission of radiation, is determined by various collisional processes involving free and bound electrons such as inverse Bremsstrahlung, photoionization, and inelastic scattering. Relative contributions of individual collision processes depend mostly on the electron temperature  $T_e$ , e.g. the inverse Bremsstrahlung is more important for higher  $T_e$ . For low temperature plasmas with  $T_e \sim 1\text{eV}$ , scattering and absorption by ice, droplets, or dust grains in the medium cannot be ignored. A number of models have been reported to analyze such inhomogeneous media containing microscopic constituents by considering the chemical equilibrium of each component across the phase boundary; that is, the first-order phase transition of a subcritical fluid is presumed [8–10].

In the present work, we demonstrate an efficient generation of long-lived high-density plasmas by applying nanosecond (ns) laser pulse on supercritical fluids (SCFs). We chose such medium for high-density plasma discharge, in part because discharge in SCFs would require less power compared to that in liquids, owing to the absence of liquid-gas phase transition, and in part because an inhomogeneous SCF can be prepared as we recently discovered that liquid-like fluid packages

(nanometer-sized clusters and sub-micrometer-sized droplets) persist for a surprisingly long time in the SCF that is obtained through a non-equilibrium process [11]. Note that the latter work breaks the conventional wisdom that an SCF is homogeneous and structureless single phase medium, and extends the related studies about liquid- or gas-like properties of SCFs in equilibrium [11–21].

In the following sections, we show that the plasma reaches and stays in the SCP state for a duration of about ten times longer than the pulse length, which alleviates the difficulty in measuring plasma parameters. The temporal evolution of plasma temperature and density is accurately measured by fitting the optical emission spectra and solving the Saha equation modified by the ionization potential reduction. In addition, we demonstrate the effect of the microscopic constituents in inhomogeneous SCFs on the plasma's opacity. Our study demonstrates an enhanced photon confinement in SCPs produced in inhomogeneous SCFs, suggesting that the phase-separated microscopic constituents play a vital role on the radiation process in SCP. The relevant examples include lightening in a thick planetary atmosphere that is instantaneously cooled and locally condensed by storms, inertial confinement fusion discharges of targets with inevitable defects from the fabrication process [22, 23], nanomaterial synthesis [24], and laser-produced plasma light sources for extreme ultraviolet (EUV) nanolithography [25–27].

## 2. Generation of jet-shaped plasma

In the process of increasing the chamber pressure up to 100 bar by controlled compression-expansion cycles of argon fluid, large populations of liquid-like fluid packages ranging in size from several nanometers (clusters) to sub-micrometer (droplets) are created (a more detailed explanation can be found in the supplementary information and [11]). The liquid-like mesoscopic particles survive in SCF for a long timescale of the order of an hour, making the medium inhomogeneous. After two hours or so, the majority of the liquid-like particles dissolve into the background, and the medium becomes homogeneous. A nanosecond laser pulse is focused into either inhomogeneous or homogeneous medium to produce dense plasma. A detailed experimental setup is described in the Methods section.

The laser pulse pre-ionizes the medium within its envelope as it propagates to the focal point. A high-density plasma blob is initially formed at the focal point and it grows toward the laser upstream, i.e. in the opposite direction to the propagation of the laser pulse. The electron density of the initial plasma exceeds the critical density of the laser's optical frequency [28] as evidenced by negligible passage of laser power onto the beam dump. That is, the laser pulse is reflected backward, further ionizing the medium in the upstream region. Thus, the laser energy is asymmetrically deposited with respect to the focus, and as a result, the plasma undergoes backward expansion (see the supplementary information). This same

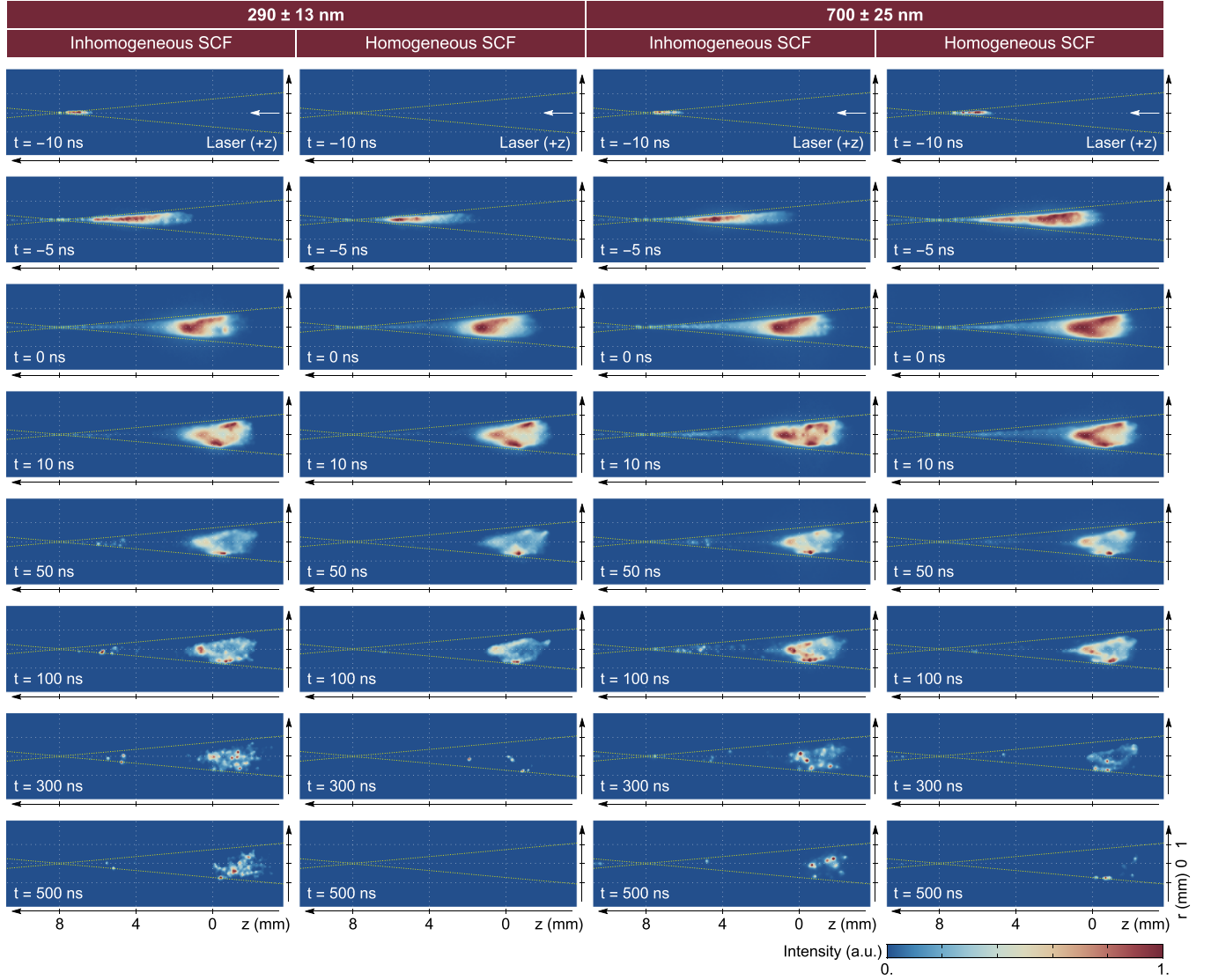


**Figure 1.** Filtered images of the plasma discharges. The first (last) two columns show the images with a bandpass filter  $290 \pm 13$  nm ( $700 \pm 25$  nm). For each filter, the images are taken under two different medium conditions (inhomogeneous and homogeneous) and are respectively normalized with respect to the maximum intensity of the two cases at each time frame. Jet-like plasma shapes are similar in both medium conditions with their boundaries following the laser beam's envelope (yellow dashed line). The plasma shape is attributed to the progressive backward expansion of the plasma absorbing the laser energy. The spectral data presented in figures 2 and 3 are taken at the spatial origin ( $r = 0$  and  $z = 0$ ).

expansion process occurs in both medium conditions and produces an elongated, jet-shaped plasma. In the ICCD images of the plasmas (figure 1), the time origin ( $t = 0$ ) and spatial origin ( $r = 0$  and  $z = 0$ ) are defined at when and where the plasma emission is the most intense, respectively.

The average expansion speed is about  $1000 \text{ km s}^{-1}$ , which is much faster than any particle diffusion and consistent with previous observations reported in literature [28, 29]. The expansion is likely due to laser absorption via inverse Bremsstrahlung process during ion-electron collisions [30]. As expected, the timescale of plasma expansion is comparable to the laser pulse duration of about 6 ns. Both the plasma density and the temperature increase from about  $t = -6$  ns until  $t = 0$  ns, and then the expansion ceases.

### 3. Strongly coupled plasma

The bulk characteristics of the plasmas in the homogeneous and inhomogeneous cases are indistinguishable in the early stage when the continuum emission is dominant over the line emissions whereas the difference due to the medium conditions emerges at later time (figure 2(a)). We analyze the optical emissions to investigate the plasma evolution and check the strongly coupled condition along the way.

We observe that continuum emissions are in the 230–640 nm spectral range and broadened line emissions in the infrared region. A similar feature has been observed in micro-discharge plasmas in liquids [31–34]. In such dense plasmas including our case, the radiation mainly arises from

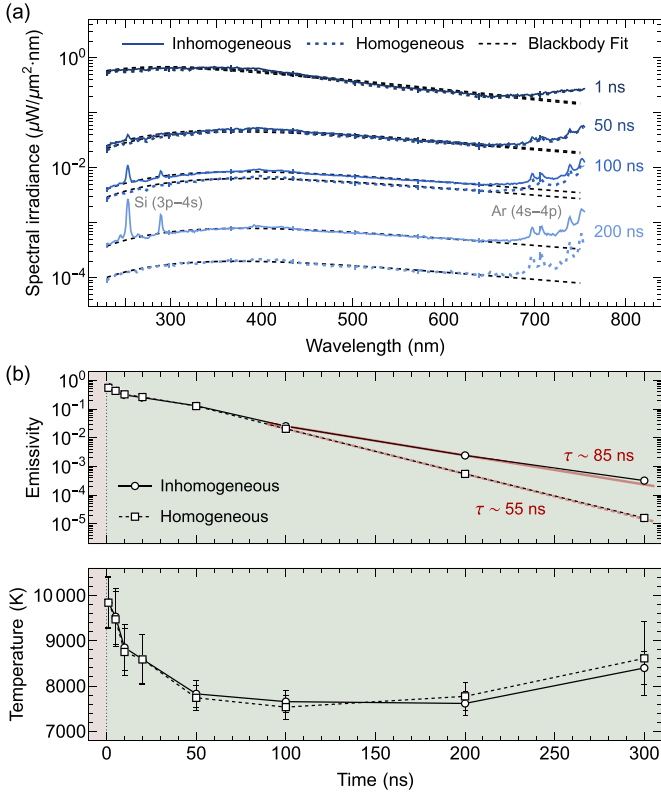


**Figure 2.** Blackbody analysis of the plasma radiation spectrum. (a) Absolutely calibrated broadband spectra from the plasmas along with the corresponding blackbody fits. The spectra are fit with the blackbody radiation model within 230–640 nm, which excludes the highly broadened argon atomic line emissions that appear in the red and near-infrared region on top of the rising baseline. The emission is mostly continuum in the early stage, and line emissions gradually increase with time. While the Ar I peaks appear for both cases, the Si I peaks are only observed in the case of inhomogeneous medium. The radiations from plasmas in different medium conditions deviate increasingly with time. (b) Emissivity and temperature of the plasmas as a function of time at the origin ( $r = 0$  and  $z = 0$ ). The emissivities for both plasmas are identical when  $t \leq 50$  ns. However, after  $t > 50$  ns, the emissivities start to deviate from each other, indicating the photon confinement of the plasma in the inhomogeneous medium exceeds that in the homogeneous medium, for identical temperature.

three-body recombination processes of electrons and ions [35], and is thermalized due to the high absorptivity of the plasma [31], yielding a blackbody emission spectrum. We use the Planck's blackbody function to fit the continuum in the 230–640 nm spectral region [31]. The spectral irradiance of an ideal blackbody is

$$I_{\text{ideal}}(\lambda; T) = \frac{2\pi hc^2}{\lambda^5 \{\exp(hc/\lambda k_B T) - 1\}}, \quad (1)$$

where  $h$ ,  $c$ ,  $\lambda$ , and  $T$  are the Planck constant, and the speed of light, the wavelength, and the blackbody temperature, respectively. The emissivity of the plasma  $\varepsilon_p$  is defined by the ratio of the radiation intensity from the plasma to that from an ideal blackbody of the same temperature,

$$I_{\text{exp}}(\lambda; T) = \varepsilon_p I_{\text{ideal}}(\lambda; T). \quad (2)$$

Hence, the closer to unity  $\varepsilon_p$  is, the closer to an ideal blackbody the plasma is. The high emissivity of the plasma in the early phase ( $t < 50$  ns) is due to the high electron density which provides high photon confinement. As the electron density decreases in the later time  $t > 50$  ns, the photon confinement and the emissivity exhibit noticeable dependence on the medium condition (which will be discussed later).

By fitting equations (1) and (2) to the continuum emissions at different times, one obtains the temporal change of the emissivity and temperature (figure 2(b)). The emissivities of the plasmas in both medium conditions are  $\sim 0.6$  initially (at  $t = 0$  ns) and decrease exponentially. The emissivities start to deviate from each other at around  $t = 100$  ns. The temperature evolution is similar in both conditions. The initial temperature is on the order of 10 000 K, rapidly decreases on a timescale of 50 ns, and slowly increases for a much longer period. Note that the radiation better fits the blackbody shape after 50 ns, resulting in smaller errors. (The confidence intervals of the fitting parameters of all data are given in the supplementary information.)

The electron density of a dense plasma can be calculated when it is transitioning from opaque to transparent, i.e. when the emissivity deduced from the blackbody spectrum first drops below unity [36, 37]. However, in our experiment, the most opaque plasma at  $t = 0$  ns has an emissivity of 0.6, incapacitating the plasma opacity analysis. Instead, we try an indirect method to estimate the electron density, which solves two coupled equations—the potential lowering equation and the corrected Saha's equation.

In high-density plasmas, collisional processes are dominant over radiative processes. De Giacomo *et al* [35] shows that three-body recombination is much faster than radiative recombination even for  $T = 10000$  K at  $n_e = 10^{21} \text{ cm}^{-3}$ . The three-body recombination timescale is only about 10 fs [35] which is much faster than the timescale of the plasma evolution in our experiment. It is then reasonable to assume establishment of Saha equilibrium among the ionization stages. For the equilibration process in dense plasmas, one must consider the reduction of ionization potential due to the Debye screening [35, 37]. The lowering of the ionization potential allows the atoms to be easily ionized, even when the photon energy (1.2 eV or 1064 nm) is much smaller than unperturbed ionization energy ( $\chi_0 \approx 15.8$  eV for Ar I). The potential lowering is roughly estimated to be on the order of 10 eV or so, which allows Ar I easily to be ionized by laser photons leading to the ionization avalanche as the electron density increases during the formation of the initial plasma.

For a more precise description, the amount of the ionization potential reduction in a dense plasma is given by

$$\Delta\chi = \frac{(\bar{Z} + 1)e^3}{4\pi\epsilon_0} \sqrt{\frac{\bar{Z}(\bar{Z} + 1)n_0}{\epsilon_0 k_B T_e}}, \quad (3)$$

where  $n_0$  is the atomic number density of the medium, and  $\bar{Z} = n_e/n_0$  is the effective ionization level [37, 38]. The Saha



equation is corrected under the presence of potential reduction accordingly:

$$\frac{x_{m+1}x_e}{x_m} = \frac{2}{n_0} \frac{u_{m+1}}{u_m} \left( \frac{m_e k_B T_e}{2\pi \hbar^2} \right)^{3/2} \exp \left( -\frac{\chi_m - \Delta\chi}{k_B T_e} \right), \quad (4)$$

where  $x_m$ ,  $x_e$ ,  $u_m$ ,  $\chi_m$ ,  $m_e$ , and  $\hbar$  are the ion concentration fraction, electron concentration fraction, electronic partition function, ionization potential for the  $m$ th ion ( $m = 0$  corresponds to the neutral atom), the electron mass, and the reduced Planck constant, respectively [37–39]. Assuming that the singly ionized argon is the dominant ion species,  $x_0 = 1 - \bar{Z}$  and  $x_1 = x_e = \bar{Z}$ , and the Saha equation (4) for  $m = 0$  becomes

$$\frac{\bar{Z}^2}{1 - \bar{Z}} = \frac{2}{n_0} \frac{u_1}{u_0} \left( \frac{m_e k_B T_e}{2\pi \hbar^2} \right)^{3/2} \exp \left( -\frac{\chi_0 - \Delta\chi}{k_B T_e} \right), \quad (5)$$

where  $\chi_0$  is the ionization potential of the isolated neutral argon atom. Solving equations (3) and (5) simultaneously using the observed plasma temperature of 10 000 K at  $t = 0$  ns in our experiments and using  $u_0 = 1$ ,  $u_1 = 5.66$ ,  $\chi_0 \approx 15.8$  eV [40], and  $n_0 = 2.53 \times 10^{21} \text{ cm}^{-3}$  for the supercritical argon fluid medium at 300 K and 100 bar [41], we obtain the degree of ionization  $\bar{Z} \approx 0.48$  and potential lowering  $\Delta\chi \approx 13$  eV. These values yield an electron density of  $n_e \approx 1.2 \times 10^{21} \text{ cm}^{-3}$  and a Coulomb coupling parameter of  $\Gamma \approx 2.9$  (see the supplementary information), showing that the plasma in the early phase is in the strongly coupled state. The strongly coupled state is maintained approximately for  $t \lesssim 50$  ns until the electron density remains sufficiently high.

The plasma relaxes out of the strongly coupled state as indicated by the exponential decrease in emissivity, which implies acceleration of electron loss. The main electron loss channel is three-body recombination as discussed earlier [35]. To check if diffusion plays any significant role, let us consider the self-diffusion coefficient  $D$  of SCP given by [36, 42]

$$D \approx D^* a^2 \omega_p, \quad (6)$$

where the Wigner–Seitz radius  $a = (4\pi n_e/3)^{-1/3} \approx 0.58$  nm, the plasma frequency  $\omega_p = \sqrt{n_e e^2 / \varepsilon_0 m_e} \approx 2.0 \times 10^{15}$  Hz, and the normalized self-diffusion coefficient  $D^* \sim 0.7$  for  $\Gamma \approx 2.9$  [42]. Therefore, for a time duration  $\Delta t = 100$  ns, the maximum diffusion length  $\Delta x \sim \sqrt{D \Delta t} \sim 7$   $\mu\text{m}$ , which is much smaller than the radial size of the plasma  $r_0 \approx 1$  mm by that time. Diffusion is thus negligible.

#### 4. Enhanced photon confinement

As time elapses, the plasma becomes diluted while the volume shrinks, and line emissions appear on top of the continuum. The argon line emissions are observed in both medium conditions as expected. Interestingly, on the other hand, silicon line emissions are observed in the spectral region of 250–300 nm only for the case of inhomogeneous medium, and are completely absent for the case of homogeneous medium. Si I

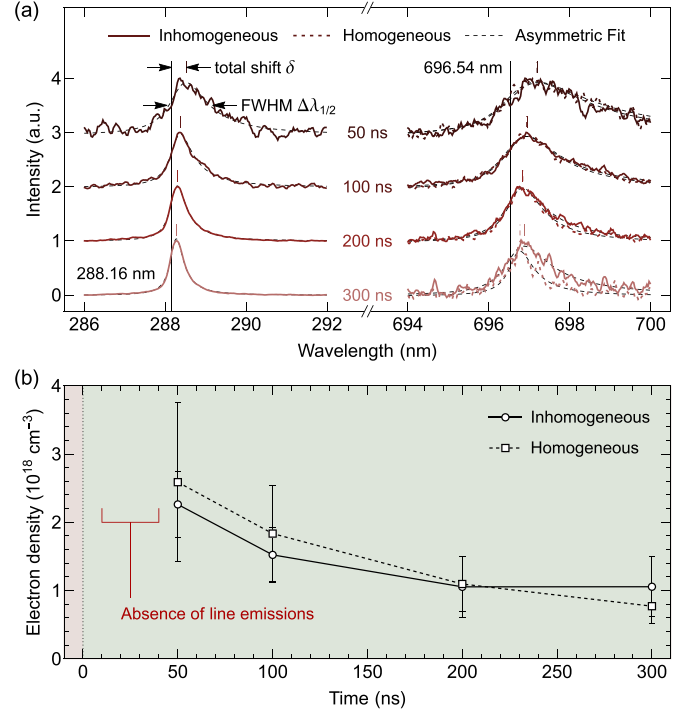


**Figure 3.** Asymmetric Stark broadenings. (a) Asymmetric Stark broadening for the Si I emission line ( $4s^1P_1^o \rightarrow 3p^1D_2$ , 288.16 nm) and the Ar I emission line ( $4p^2[1/2]_1 \rightarrow 4s^2[3/2]_2^o$ , 696.54 nm). The silicon line emission is only observed for the plasma generated in the inhomogeneous medium, whereas the argon line emission is detected for both conditions. The total broadening and shift decrease with time. At 1000 ns, the argon line emissions disappear for both medium conditions. (b) Temporal evolution of electron density. The electron densities of the plasmas in both media are of the same order in contrast to the large difference of the plasma emissivities. The error bars show the standard deviations of the Stark broadening analysis results based on the total shifts and widths of the silicon and argon lines.

line emissions are due to Si-containing impurity molecules that are expected to originate from the lubricant oil in the compressor. A trace amount of oil vapor can permeate into the high-pressure chamber during the compression-expansion process. The impurity molecules can provide the nucleation sites for the formation of liquid-like fluid packages and would float with them until they dissolve. It appears that the impurity molecules diffuse away and stick to the wall by the time that the supercritical medium becomes homogeneous. The existence of Si impurities is fortunate rather than being a nuisance because a trace amount of Si can generate high intensity optical emissions owing to the high transition strengths of many energy levels of the neutral Si atom. Thus, we utilize the Si line emissions to measure the electron density at a later time ( $t \geq 50$  ns) when the plasma becomes diluted (figure 3) and the electron density estimation by the modified Saha equation becomes unviable.

A large asymmetric Stark broadening is observed in both the silicon and argon line emissions. It is well known that the asymmetry originates from the influence of the static ions

[43, 44]. The line profile considering both electron and ion Stark effects is given by [43, 45]

$$j_A(\bar{\lambda}) = \int_0^\infty \frac{H(\beta)d\beta}{1 + (x - A^{4/3}\beta^2)^2}, \quad (7)$$

where  $j_\alpha$  is the relative intensity of the profile;  $H(\beta)$  is the microfield strength at the emitting neutral atom as a function of the reduced field strength  $\beta$ ;  $A$  is the ion broadening parameter which is a measure of the ion contribution to the asymmetry (also known as  $\alpha$ );  $\bar{\lambda} = \pm(\lambda - \lambda_0 - d_e)/w_e$  is the reduced wavelength and the sign determines the direction of the asymmetry (for a positive sign, the asymmetric tail stretches out to the longer wavelength);  $\lambda_0$ ,  $d_e$ , and  $w_e$  are the center wavelength of unperturbed line emission, the electron impact shift, and the electron impact width, respectively. The asymptotic approximation to the microfield strength yields

$$H(\beta) \approx \tilde{K}\beta^{-5/2} \exp\left(-\tilde{\Gamma}\beta^{1/2} - \beta^{-3/2}\right), \quad (8)$$

where  $\tilde{K}$  is determined from the normalization constraint, whereas  $\tilde{\Gamma}$  is a free parameter close to  $\Gamma$  [46]. For our analysis, we choose  $\tilde{\Gamma} \approx 0.35$  using the approximate plasma parameters  $n_e = 10^{18} \text{ cm}^{-3}$  and  $T_e = 8000 \text{ K}$  with the corresponding Coulomb coupling parameter  $\Gamma = 0.34$  and noting that the fitting function is not very sensitive to the value of  $\tilde{\Gamma}$ . The total shift and width of the line emissions are obtained by fitting the measured line profile using equations (7) and (8), and then the electron densities are estimated (figure 3(b)) by comparing them with the literature [45, 47]. Note that the instrumental broadening of 0.45 nm is negligible, compared to the Stark effect (larger than 0.8 nm except for Si I lines when  $t \geq 200 \text{ ns}$  which are excluded for this analysis) as shown in figure 3(a).

The estimated electron density of the plasma after 50 ns is on the order of  $10^{18} \text{ cm}^{-3}$  for both SCF medium conditions. Even though the inherent error is large in the Stark broadening analysis, we can infer that the electron densities for both medium conditions are of the same order. However, even under similar electron densities, the emissivity of the plasma generated in the inhomogeneous SCF surpasses the case of the homogeneous SCF by an order of magnitude at  $t = 300 \text{ ns}$  (figure 2(b)). As previously mentioned, the medium condition affects the photon confinement more significantly than the electron density when the electron density becomes low in the relaxation stage ( $t > 50 \text{ ns}$ ).

The integrated extinction coefficient of plasma bulk along the line of sight  $\alpha r_0$  (where  $r_0$  is the radius of the plasma) is equal to the total emissivity of the plasma  $\varepsilon r_0 = \varepsilon_p$  when the object is in thermal equilibrium [48] according to Kirchhoff's law of thermal radiation. Using the radius of the plasma  $r_0 \approx 1 \text{ mm}$  and the extinction coefficient of the inhomogeneous SCF  $\alpha_{\text{inhomo}} \approx 0.005 \text{ mm}^{-1}$  [11] in our experiment,  $\alpha_{\text{inhomo}} r_0 = 0.005$  (note that the absorption and scattering of the homogeneous medium is negligible). This estimation supports the experimental observation after  $t = 50 \text{ ns}$ : the separation of emissivity between the different medium conditions without compelling differences in electron density and temperature (figure 2(b)). Microscopically, the high extinction

coefficient of the inhomogeneous SCF mainly comes from the scattering by the nanometer-sized argon clusters [11].

One last feature of the plasma from the inhomogeneous medium before the radiation completely disappears is that the light emission emanates from the sub-micrometer-sized droplets floating in the medium (see the images for  $t \geq 300 \text{ ns}$  in figure 1). This suggests that the droplets inside the plasma act as recombination sites because atomic line emissions follow from electron-ion recombination. Therefore, the particles submerged in SCP attract a considerable amount of electrons and serve as the charge reservoirs. The charge in dusty plasma is understood based on the unequal charge flow of electrons and ions at the dust surface [49] is still applicable in this case. Therefore, once an SCP is generated, electrons are attracted to the droplets, and the recombinations with ions that occur at later times are localized near the droplets.

## 5. Conclusion

We showed that the single-component SCF is an energy-efficient medium for generation of high-density SCP plasmas by laser pulse, as there is no latent heat associated with temperature changes during the discharge process. Furthermore, we revealed that the liquid-like mesoscopic particles in the phase-separated inhomogeneous SCF [11] enhance the confinement of radiation from the plasma. Recalling that the major uncertainty in modeling the opacity of fluids in a subcritical condition originates from phase transitions when the temperature and density change (chapter 6 in [7]), our experiment suggests a new research area for dusty SCFs. This finding may also provide a method of increasing the brightness and duration of light emission from a dense plasma. In particular, considering the fact that the Rayleigh scattering cross-section is inversely proportional to the fourth power of the wavelength, it can be expected that the nanometer-sized clusters in the medium create a more effective optical confinement to applications for short wavelengths such as EUV or x-ray generation by laser-produced plasmas. In addition, SCPs in such inhomogeneous SCFs may be a good platform to study other anomalous transport properties regarding charge or heat.

## 6. Methods

### 6.1. Experimental setup

The SCP is generated using an Nd:YAG pulse laser (Quantel)—wavelength: 1064 nm, pulse energy: 730 mJ/pulse, duration: 6 ns, and operation frequency: 2 Hz. The laser repetition rate is set to avoid the residual turbulence of the medium from successive pulses (see the supplementary information). The laser is focused with a 50 mm AR coated plano-convex lens (Thorlabs) into the high-pressure chamber and the final intensity at focus is estimated to be on the order of  $10^{12} \text{ W cm}^{-2}$  (detailed analysis is given in the supplementary information). The cube-shaped stainless steel chamber has five optical viewports, each of which consists of a sapphire window and stainless steel housing (Rayotek).

The light emission from the plasma is guided by a lens and an optical fiber (Thorlabs)—collection area:  $\sim 0.43 \text{ mm}^2$  to the Czerny-Turner type monochromator (Princeton Instruments)—focal length: 300 mm and ICCD (Princeton Instruments). The ICCD camera is synchronized with the electrical signal that precedes the Q-switch of the Nd:YAG laser. The gate of ICCD opens at the rising edge of the trigger signal (timing jitter  $< 1 \text{ ns}$ ). Regardless of the gate width, the time delay of each experiment refers to the gate opening event. For instance, if the time delay  $t = 300 \text{ ns}$  and the gate width  $w = 30 \text{ ns}$ , the ICCD acquires the signal from 300 to 330 ns. The gate width of ICCD is manipulated from 3 to 50 ns depending on the time delay, and each spectrum is averaged over 10–600 plasma discharges to improve the signal-to-noise ratio (the supplementary information includes a detailed description of acquisitions). The shot-to-shot fluctuation of the laser pulse is negligible, and that of the plasma emission is less than 20%. The spectral response of the measurement system is absolutely calibrated by using a standard light source to 15% of errors (Ocean Optics). The filtered image of plasma discharge is taken separately with the imaging optics and ICCD. All images presented in figure 1 are single-shot images without averaging.

### 6.2. Radiative transfer equation

The radiative transfer for an emitting and absorbing medium by incorporating both effects into a single equation along a ray is given by [31, 48]

$$\frac{dI_\lambda}{ds} = -\alpha_\lambda I_\lambda + \alpha_\lambda B_\lambda(T), \quad (9)$$

where  $s$ ,  $I_\lambda$ ,  $\alpha_\lambda$ , and  $B_\lambda(T)$  are the distance, the spectral irradiance, the net absorptivity per unit distance (also called the extinction coefficient to distinguish it from the ‘true’ absorption coefficient which excludes the scattering effects [48]), and the Planck function, respectively. If we choose a boundary condition  $I_\lambda(0) = 0$ , which implies the light emission at the starting point is zero because there is no emitter and the emission gradually integrated along with the line of sight, equation (9) yields

$$I_\lambda(s) = \{1 - e^{-\alpha_\lambda s}\} B_\lambda(T). \quad (10)$$

For a gray-body plasma where  $\alpha_\lambda s \ll 1$ , equation (10) is reduced to  $I_\lambda(s) \approx \alpha_\lambda s B_\lambda(T)$ . By the Kirchhoff’s law of thermal radiation, when the object is in thermal equilibrium, the extinction coefficient and emissivity is identical ( $\alpha_\lambda = \varepsilon_\lambda$ ). Considering the line integrated emissivity  $\varepsilon_\lambda s = \varepsilon_p$ , we have  $I_\lambda = \varepsilon_p B_\lambda(T)$ , which is identical to equation (2).

### Data availability statement

The data that support the findings of this study are available upon reasonable request from the authors.

### Acknowledgments

This work was supported by the National Research Foundation of Korea (NRF) funded by the Ministry of Science and ICT (Nos. 2019R1A2C3011474, 2022M3H4A1A04074153, 2019R1A2C1004862, and 2021-SRETC-P01-2) and Ministry of Education (No. 2019R1A6A3A13091407).

### Code availability

The codes used for analysis are available from the corresponding author upon reasonable request.

### Author contributions

G Y proposed the original idea and conceived the project. S L and J L designed the high-pressure laser-produced plasma system and performed the experiments. S L and J L carried out the majority of the data processing, and S L developed the density estimation method from the potential lowering effect and Saha’s equation. Y D Y provided the theoretical analysis. G Y and D E K supervised the project. All authors contributed significantly to the discussion of the results. S L wrote the manuscript with input from all coauthors.

### Conflict of interest

The authors declare no competing interests.

### ORCID iDs

Seungtaek Lee  <https://orcid.org/0000-0002-3292-4967>  
 Juho Lee  <https://orcid.org/0000-0002-0676-5405>  
 Young Dae Yoon  <https://orcid.org/0000-0001-8394-2076>  
 Gunsu Yun  <https://orcid.org/0000-0002-1880-5865>

### References

- [1] Ichimaru S 1977 Theory of strongly correlated charged-particle systems: plasma turbulence and high-density electron liquids *Phys. Rev. A* **15** 744
- [2] Murillo M S 2004 Strongly coupled plasma physics and high energy-density matter *Phys. Plasmas* **11** 2964–71
- [3] Castello Lucco F 2021 Bridge functions in strongly coupled plasmas: theory, simulations and applications *PhD Dissertation* KTH Royal Institute of Technology
- [4] Ichimaru S 1982 Strongly coupled plasmas: high-density classical plasmas and degenerate electron liquids *Rev. Mod. Phys.* **54** 1017
- [5] Cartier K 2020 Planetary lightning: same physics, distant worlds *Eos* **101** 22–27
- [6] Remington B A, Drake R P and Ryutov D D 2006 Experimental astrophysics with high power lasers and Z pinches *Rev. Mod. Phys.* **78** 755
- [7] Huebner W F and Barfield W D 2014 *Opacity* (Berlin: Springer)
- [8] Cameron A and Pine M 1973 Numerical models of the primitive solar nebula *Icarus* **18** 377–406
- [9] Pollack J B, Hollenbach D, Beckwith S, Simonelli D P, Roush T and Fong W 1994 Composition and radiative



- properties of grains in molecular clouds and accretion disks *Astrophys. J.* **421** 615–39
- [10] Alexander D, Rypma R L and Johnson R 1983 Effect of molecules and grains on rosseland mean opacities *Astrophys. J.* **272** 773–80
- [11] Lee S, Lee J, Kim Y, Jeong S, Kim D E and Yun G 2021 Quasi-equilibrium phase coexistence in single component supercritical fluids *Nat. Commun.* **12** 4630
- [12] Simeoni G, Bryk T, Gorelli F, Krisch M, Ruocco G, Santoro M and Scopigno T 2010 The widom line as the crossover between liquid-like and gas-like behaviour in supercritical fluids *Nat. Phys.* **6** 503–7
- [13] Gorelli F, Santoro M, Scopigno T, Krisch M and Ruocco G 2006 Liquidlike behavior of supercritical fluids *Phys. Rev. Lett.* **97** 245702
- [14] Banuti D 2015 Crossing the widom-line–supercritical pseudo-boiling *J. Supercrit. Fluids* **98** 12–16
- [15] Maxim F, Contescu C, Boillat P, Niceno B, Karalis K, Testino A and Ludwig C 2019 Visualization of supercritical water pseudo-boiling at widom line crossover *Nat. Commun.* **10** 4114
- [16] Pipich V and Schwahn D 2018 Densification of supercritical carbon dioxide accompanied by droplet formation when passing the widom line *Phys. Rev. Lett.* **120** 145701
- [17] Pipich V and Schwahn D 2020 Polymorphic phase transition in liquid and supercritical carbon dioxide *Sci. Rep.* **10** 11861
- [18] Prescher C, Fomin Y D, Prakashenka V, Stefanski J, Trachenko K and Brazhkin V 2017 Experimental evidence of the Frenkel line in supercritical neon *Phys. Rev. B* **95** 134114
- [19] Bryk T, Gorelli F, Mryglod I, Ruocco G, Santoro M and Scopigno T 2017 Behavior of supercritical fluids across the “Frenkel line” *J. Phys. Chem. Lett.* **8** 4995–5001
- [20] Ploetz E A and Smith P E 2019 Gas or liquid? The supercritical behavior of pure fluids *J. Phys. Chem. B* **123** 6554–63
- [21] Schienbein P and Marx D 2018 Investigation concerning the uniqueness of separatrix lines separating liquidlike from gaslike regimes deep in the supercritical phase of water with a focus on widom line concepts *Phys. Rev. E* **98** 022104
- [22] Clark D S, Haan S W, Hammel B A, Salmonson J D, Callahan D A and Town R P J 2010 Plastic ablator ignition capsule design for the national ignition facility *Phys. Plasmas* **17** 052703
- [23] Wang T, Du K, He Z and He X 2017 Development of target fabrication for laser-driven inertial confinement fusion at research center of laser fusion *High Power Laser Sci. Eng.* **5** E5
- [24] Stauss S, Muneoka H, Urabe K and Terashima K 2015 Review of electric discharge microplasmas generated in highly fluctuating fluids: characteristics and application to nanomaterials synthesis *Phys. Plasmas* **22** 057103
- [25] Sokolowski-Tinten K, Bialkowski J, Cavalleri A, von der Linde D, Oparin A, Meyer-ter-Vehn J and Anisimov S 1998 Transient states of matter during short pulse laser ablation *Phys. Rev. Lett.* **81** 224
- [26] Von der Linde D and Sokolowski-Tinten K 2000 The physical mechanisms of short-pulse laser ablation *Appl. Surf. Sci.* **154–155** 1–10
- [27] Klein A L, Bouwhuis W, Visser C W, Lhuissier H, Sun C, Snoeijer J H, Villiermaux E, Lohse D and Gelderblom H 2015 Drop shaping by laser-pulse impact *Phys. Rev. Appl.* **3** 044018
- [28] Harilal S S, Brumfield B E and Phillips M C 2015 Lifecycle of laser-produced air sparks *Phys. Plasmas* **22** 063301
- [29] Bataller A, Putterman S, Pree S and Koulakis J 2016 Observation of shell structure, electronic screening and energetic limiting in sparks *Phys. Rev. Lett.* **117** 085001
- [30] Delone N B 1993 *Basics of Interaction of Laser Radiation with Matter* (Gif-sur-Yvette: Atlantica Séguier Frontières)
- [31] Yasui K 1999 Mechanism of single-bubble sonoluminescence *Phys. Rev. E* **60** 1754
- [32] Flannigan D J and Suslick K S 2005 Plasma formation and temperature measurement during single-bubble cavitation *Nature* **434** 52–55
- [33] Hopkins S D, Putterman S J, Kappus B A, Suslick K S and Camara C G 2005 Dynamics of a sonoluminescing bubble in sulfuric acid *Phys. Rev. Lett.* **95** 254301
- [34] Kappus B, Bataller A and Putterman S 2013 Energy balance for a sonoluminescence bubble yields a measure of ionization potential lowering *Phys. Rev. Lett.* **111** 234301
- [35] De Giacomo A, Gaudioso R, Dell’Aglia M and Santagata A 2010 The role of continuum radiation in laser induced plasma spectroscopy *Spectrochim. Acta B* **65** 385–94
- [36] Dimonte G and Daligault J 2008 Molecular-dynamics simulations of electron-ion temperature relaxation in a classical coulomb plasma *Phys. Rev. Lett.* **101** 135001
- [37] Bataller A, Plateau G, Kappus B and Putterman S 2014 Blackbody emission from laser breakdown in high-pressure gases *Phys. Rev. Lett.* **113** 075001
- [38] Griem H R 1962 High-density corrections in plasma spectroscopy *Phys. Rev.* **128** 997
- [39] Zeldovich Y B 1967 Theory of shock waves and introduction to gas dynamics *Technical Report* (OH: Foreign Technology Div Wright-Patterson AFB)
- [40] Kramida A, Ralchenko Y and Reader J 2020 *NIST Atomic Spectra Database, NIST Standard Reference Database Number 78* (Gaithersburg, MD: National Institute of Standards and Technology)
- [41] Linstrom P J and Mallard W G 2020 *NIST Chemistry Webbook, NIST Standard Reference Database Number 69* (Gaithersburg, MD: National Institute of Standards and Technology)
- [42] Baalrud S D and Daligault J 2013 Effective potential theory for transport coefficients across coupling regimes *Phys. Rev. Lett.* **110** 235001
- [43] Bengoechea J, Aragón C and Aguilera J 2005 Asymmetric stark broadening of the Fe I 538.34 nm emission line in a laser induced plasma *Spectrochim. Acta B* **60** 897–904
- [44] Ivković M and Konjević N 2017 Stark width and shift for electron number density diagnostics of low temperature plasma: application to silicon laser induced breakdown spectroscopy *Spectrochim. Acta B* **131** 79–92
- [45] Griem H 2012 *Spectral Line Broadening by Plasmas* (Amsterdam: Elsevier)
- [46] Potekhin A Y, Chabrier G and Gilles D 2002 Electric microfield distributions in electron-ion plasmas *Phys. Rev. E* **65** 036412
- [47] Konjević N, Lesage A, Fuhr J R and Wiese W L 2002 Experimental stark widths and shifts for spectral lines of neutral and ionized atoms (a critical review of selected data for the period 1989 through 2000) *J. Phys. Chem. Ref. Data* **31** 819–927
- [48] Rybicki G B and Lightman A P 1991 *Radiative Processes in Astrophysics* (New York: Wiley)
- [49] Bellan P M 2008 *Fundamentals of Plasma Physics* (Cambridge: Cambridge University Press)